

# Perovskite Photovoltaic Devices with Carbon-Based Electrodes Withstanding Reverse-Bias Voltages up to $-9$ V and Surpassing IEC 61215:2016 International Standard

Dmitry Bogachuk, Karima Saddedine, David Martineau, Stephanie Narbey, Anand Verma, Paul Gebhardt, Jan P. Herterich, Nico Glissmann, Salma Zouhair, Jochen Markert, Isaac E. Gould, Michael D. McGehee, Uli Würfel,\* Andreas Hinsch, and Lukas Wagner\*

One of the key challenges of perovskite photovoltaics (PV) is the long-term stability. Although efforts are made to improve the lifetime of perovskite PV devices, their degradation under reverse-bias conditions is barely addressed. Herein, perovskite solar cells with carbon-based electrodes are presented which demonstrate superior resilience against reverse-bias-induced degradation. Although their breakdown voltage is identified to be at approximately  $-3.6$  V, cells do not degrade until the applied reverse-bias exceeds  $-9$  V. Two main degradation mechanisms are identified: 1) iodine loss due to hole tunneling into perovskite, which takes place even at low reverse-bias but decomposes the perovskite only after long time durations; and 2) rapid heating at large reverse-bias leading to formation of  $\text{PbI}_2$ , which starts at shunts and then follows the path of the least resistance for the cell current, which is primarily influenced by the electrode sheet resistances. Finally, perovskite solar modules with carbon-based electrodes are demonstrated, which are subjected to a “hotspot” test described in the IEC 61215:2016 international standard at an accredited module testing laboratory. Passing this accelerated test for the first time confirms the superior stability of perovskite PV devices with carbon-based electrodes and highlights their large industrialization potential.

## 1. Introduction


Countless researchers across the scientific world have been attracted by perovskite materials, which exhibit favorable properties for their applications in semiconductor devices,<sup>[1–3]</sup> particularly, in photovoltaics (PV).<sup>[4–10]</sup> Although the power conversion efficiency (PCE) of perovskite solar cells (PSCs) already reached comparable values of those in conventional silicon-based PV cells,<sup>[11,12]</sup> the device stability (intrinsic and extrinsic) is still a challenge on which tremendous efforts in the perovskite community are currently focused.<sup>[13–18]</sup>

Numerous different strategies have been demonstrated to improve the stability of PSCs under conditions described in the IEC 61215:2016 international standard,<sup>[19]</sup> which represents a benchmark for commercializing any emerging PV technology and is composed of several accelerated aging tests to determine the operational

D. Bogachuk, K. Saddedine, P. Gebhardt, J. P. Herterich, N. Glissmann, S. Zouhair, J. Markert, U. Würfel, A. Hinsch, L. Wagner  
Fraunhofer Institute for Solar Energy Systems ISE  
Heidenhofstr. 2, 79110 Freiburg, Germany  
E-mail: uli.wuerfel@ise.fraunhofer.de; lukas.wagner@ise.fraunhofer.de

D. Martineau, S. Narbey, A. Verma  
Solaronix SA  
Rue de l'Ouriette 129, 1170 Aubonne, Switzerland

J. P. Herterich, U. Würfel  
Materials Research Center FMF  
University of Freiburg  
Stefan-Meier-Str. 21, 79104 Freiburg, Germany

 The ORCID identification number(s) for the author(s) of this article can be found under <https://doi.org/10.1002/solr.202100527>.

© 2021 The Authors. Solar RRL published by Wiley-VCH GmbH. This is an open access article under the terms of the Creative Commons Attribution License, which permits use, distribution and reproduction in any medium, provided the original work is properly cited.

DOI: 10.1002/solr.202100527

S. Zouhair  
FSTT  
Thin Films & Nanomaterials Lab  
Abdelmalek Essaadi University  
Tangier 90000, Morocco

I. E. Gould, M. D. McGehee  
National Renewable Energy Laboratory  
Golden, CO 80401, USA

I. E. Gould  
Materials Science and Engineering  
University of Colorado  
Boulder, CO 80309, USA

M. D. McGehee  
Department of Chemical and Biological Engineering  
University of Colorado  
Boulder, CO 80309, USA

stability of a PV module.<sup>[20]</sup> Most of the reports have primarily focused on passing the damp-heat test (85 °C, 85% RH, 1000 h)<sup>[21–24]</sup> and continuous 1 sun illumination test (AM1.5G, 1000 h).<sup>[21,25–30]</sup> There are also few works demonstrating the humidity-freeze test (10 cycles of temperature variation from –40 to 80 °C at 85% RH),<sup>[24]</sup> thermal cycling tests (50 cycles of temperature variation from –40 to 85 °C),<sup>[21,22,31]</sup> and UV-pre-exposure tests (15 kWh m<sup>–2</sup> dose of UV-light)<sup>[21,22,32]</sup> which are also required by the IEC 61215:2016 standard.

However, up to now only few works have focused on the reverse-bias-induced degradation, understanding its nature<sup>[33,34]</sup> and developing strategies to suppress it,<sup>[35]</sup> while the issue of hotspot creation and bypass diode thermal tests for perovskite solar modules (PSMs) have still not been investigated, according to our knowledge. In fact, the authors of these works<sup>[33–35]</sup> demonstrated that perovskite solar cells rapidly degrade even under mild reverse-bias conditions, highlighting that this issue is critical for the bringing perovskite PV to the market. It is surprising to see that the reverse-bias behavior of perovskite PV has been so greatly overlooked, considering that the creation of hotspots (which occur when PV device operates under reverse-bias) is one of the key challenges for the well-established PV technologies, such as silicon PV.<sup>[20]</sup> Defective or current mismatched PV cells can be considered as the intrinsic origins of the creation of hotspots in modules, while partial shading of a PV module during its operation is considered an extrinsic and often occurring cause of reverse-bias-induced degradation.<sup>[20]</sup> Therefore, if perovskite PV module manufacturers plan to contribute to sustainable electrical energy infrastructure, they need to find solutions to pass the reverse-bias test.

In this work, we systematically investigate the reverse-bias behavior of the perovskite solar cells with carbon-based back-electrode (C-PSCs), which exhibit exceptional resilience to the reverse-bias-induced degradation. Although the breakdown voltage of the single cell was identified to be around –3.6 V, these cells were proven to successfully withstand higher reverse-bias voltages and even current densities close to 70 mA cm<sup>–2</sup> when fully shaded. The impressive stability under reverse-bias is attributed to lack of metal-induced degradation mechanisms (electrode melting and metal ion diffusion at elevated temperatures), phase segregation, and degradation of organic charge extraction layers.

Furthermore, we manufacture 10 × 10 cm<sup>2</sup> perovskite solar module with carbon-based back-contacts, which we subjected to the hotspot tests (according to norms for silicon-based PV and thin-film-based PV modules) described in IEC 61215-2:2016 standard. To the best of our knowledge, these are the first published certified tests addressing the reverse-bias-induced degradation in perovskite PV modules. As our modules have successfully passed these accelerated ageing tests, this study represents a breakthrough in tackling the challenge of reverse-bias-induced degradation, thus bringing the perovskite solar cells closer to commercialization.

## 2. Results and Discussion

### 2.1. Dark *J–V* Curves of Perovskite Solar Cells with Carbon-Based Contacts

The standard device characterization of solar cells is the measurement of the *I–V* curve under illumination in a forward-bias regime between applied positive voltages  $V_a = 0$  (i.e., short-circuit) and  $V_a = V_{OC}$  (i.e., open-circuit). In the reverse-bias regime, however, the  $V_a$  is negative and the larger  $V_a$  leads to a higher potential difference between electron and hole quasi-Fermi levels (although in PSCs it is also influenced by an additional ion-induced electric field at interfaces<sup>[36]</sup>). Throughout the article we will always refer to the absolute voltage value in the context of applied reverse-bias, i.e., high reverse-bias means more negative voltage values. If the reverse-bias voltage is high enough, the conduction and valence bands of perovskite are bent stronger and at a certain point the peak electric field will exceed breakdown threshold causing large currents to flow under negative voltages<sup>[37]</sup> (which will be discussed in more detail in Section 2.4). The voltage at which breakdown occurs is referred to as breakdown voltage ( $V_{br}$ ) and it is a critical parameter for the design of photovoltaic modules.<sup>[38]</sup>

The C-PSCs utilized in this work are composed of compact titanium dioxide (c-TiO<sub>2</sub>) coated on fluorine-doped tin oxide (FTO) substrate, with a mesoporous titanium dioxide (m-TiO<sub>2</sub>) as electron selective layer (ESL), zirconium dioxide (ZrO<sub>2</sub>) insulating spacer layer, and a carbon-based electrode (Figure 1a). We note that this architecture does not include a hole selective layer

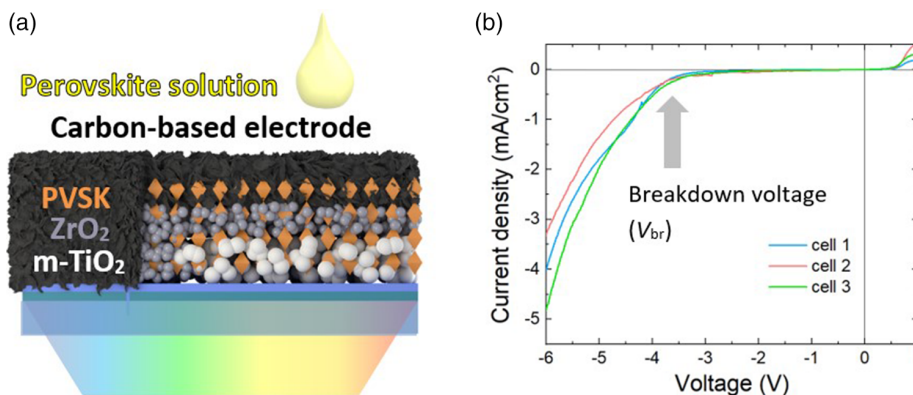


**Figure 1.** a) Architecture of perovskite solar cell with carbon-based electrode. b) Dark *I–V* measurements of C-PSCs, displaying a breakdown voltage at around –3.6 V.

(HSL). After the back-electrode is deposited, the entire mesoporous stack is infiltrated with perovskite solution, which crystallizes into  $5\text{AVA}_{1-x}(\text{CH}_3\text{NH}_3)_x\text{PbI}_3$  perovskite (where  $0 < x < 1$  and 5AVA denotes 5-aminovaleric acid) after annealing. Although, it has been demonstrated that the  $\text{CH}_3\text{NH}_3$ -based perovskite films in solar cells with standard n-i-p or p-i-n architectures are prone to degradation (e.g., thermal, under illumination<sup>[13,39,40]</sup>), when such perovskites are integrated into a C-PSC structure, the cells exhibit 9000–10 000 h of operational stability under full sun (AM1.5G spectrum) illumination at 55 °C, which are the longest stability measurements to date.<sup>[21,41]</sup> This highlights that even with  $\text{CH}_3\text{NH}_3$ -based photoabsorber, C-PSCs display superior stability and resilience to degradation under various ambient conditions.

We start investigating the reverse-bias behavior of C-PSCs by measuring the dark  $I$ - $V$  curves, primarily in the reverse-bias regime. The  $I$ - $V$  curves (from 1 to -6 V) of the manufactured cells are presented in Figure 1b. We note that, according to our knowledge, there have not been reports of reverse-bias testing of PSCs up to such large reverse-bias voltages.

From the dark  $I$ - $V$  measurement we identify the breakdown voltage to be at around -3.5 to -3.7 V which is higher than the values demonstrated in the literature, regarding reverse-bias behavior of perovskite solar cells (which are typically between -1 and -3 V).<sup>[33,34]</sup> Remarkably, the  $I$ - $V$  measurements of illuminated cells before and after the dark  $I$ - $V$  sweeps show no signs of degradation as can be inferred from invariable device performance (Figure S1, Supporting Information). Moreover, performing an  $I$ - $V$  sweep of an illuminated cell until various negative voltages also does not cause degradation (Figure S2, Supporting Information). However, we observed that the larger applied negative bias during  $I$ - $V$  scan was, the longer it took for the  $V_{\text{OC}}$  to recover (Figure S3, Supporting Information).

## 2.2. Mimicking the Behavior of a Module with Partially Shaded Subcell

Next, we study the behavior of modules by series connection of individual solar cells. Therefore, we first investigate shading effects of single cells. The  $I$ - $V$  curves of solar cells illuminated on the entire active cell area (1.44 cm<sup>2</sup>) and on a masked area (0.096 cm<sup>2</sup>) are shown in Figure S4, Supporting Information. We attribute the strong difference in FF to an increased series resistance loss for fully illuminated devices, which is a typical challenge in up-scaling solar cells. In turn, the lower  $V_{\text{OC}}$  of the masked cell can be explained by the nonilluminated area of the cell which is a passive volume that does not contribute to charge carrier generation but still causes nonradiative recombination.<sup>[42]</sup>

As photovoltaic modules are typically composed of subcells (cells connected in series forming a string of a module), we investigate the behavior of series-interconnected C-PSCs (Figure 2a), thus mimicking a perovskite PV module with carbon-based counter electrodes. The  $I$ - $V$  curves of C-PSCs connected in series, forming a string of up to six subcells is shown in Figure 2b, where we subsequently added one subcell after another. In this case, the total  $V_{\text{OC}}$  is equal to the sum of  $V_{\text{OC}}$ s of each individual subcell. The apparent decrease in fill factor (FF) is a main challenge for series-connected modules and can

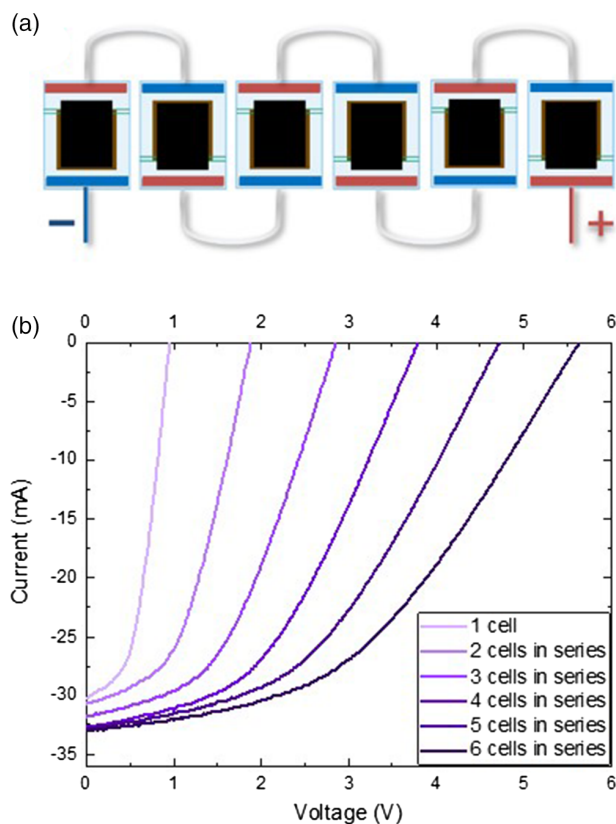


**Figure 2.** a) Illustration of the series-interconnected C-PSCs, mimicking behavior of a string in a module with six subcells. b) The  $I$ - $V$  curves of the series-interconnected cells under illumination.

be attributed to additional series resistance losses from the subcells and the external interconnection (Figure S5, Supporting Information). Although the  $I_{\text{SC}}$  in series-interconnected subcells should be limited by the lowest  $I_{\text{SC}}$  in the circuit, here the  $I_{\text{SC}}$  slightly increases with the number of connected subcells. This peculiar effect might be due to a relatively low shunt resistance (as can be seen from the  $I$ - $V$  slope at  $V=0$ ), which causes an increase in  $I_{\text{SC}}$ , even though it should normally not increase with high-performing subcells.

If one of the series-connected subcells is shaded, it is reverse-biased with photovoltage from the other unshaded subcells. In the  $I$ - $V$  plot, this is equivalent with mirroring the  $I$ - $V$  curve at the  $I$  axis. The operating point of the shaded subcell is represented by the intersection between the  $I$ - $V$  curves of the (transposed) shaded and the unshaded subcells.<sup>[38,43,44]</sup> In Figure 3a, we illustrate a situation when one of the interconnected subcells is fully shaded (thus producing a dark  $I$ - $V$  curve, which was shown in Figure 1b) and the other five unshaded subcells act as a reverse-bias voltage source on the shaded one. It can be clearly seen that the operating point shifts to higher voltages with higher number of unshaded subcells in the string.

The behavior of complete shading of one subcell in a string is shown in Figure S6, Supporting Information. When five out of six subcells in a string are fully shaded, the string produces no net current, as it is normally dominated by the smallest current

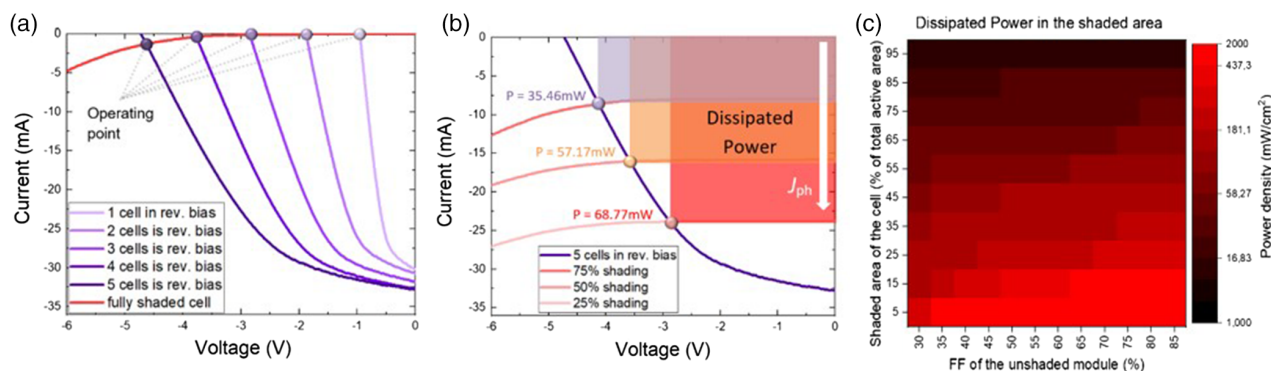


**Figure 3.** a) Illustration of  $I$ - $V$  curve produced by six series-interconnected C-PSCs, where one cell is fully shaded (producing an  $I$ - $V$  curve shown in Figure 1b), forcing the other (1–5) unshaded cell(s) to act as a reverse-bias voltage source. This representation is based on the measured  $I$ - $V$  curves in Figure 2b, which were mirrored across the  $I$  axis to mimic a reverse-bias voltage source. The operating point of the string in this case would be at the intersection between the shaded and unshaded cells. b) Illustration of the operating point dependency (and thus dissipated power) on the shaded area, which influences the photocurrent  $J_{ph}$ . c) Simulated heatmap, visualizing the influence of the shaded area and FF of unshaded module (in this example only six subcells were considered) on the dissipated power in the shaded area. The heatmap was constructed based on the operating points of simulated unshaded interconnected five subcells and one partially shaded cell, presented in Figure S8, Supporting Information. Note that the scale is logarithmic.

in the string. However, as the number of shaded subcells decreases, the current becomes higher than zero, where in the case of one nonshaded subcell and five shaded ones, the  $I_{SC}$  becomes around 11.3 mA. This peculiar phenomenon implies that even when one of the subcells in the module is fully shaded, the string can still produce some output power even without a bypass diode (although output power would be rather small). When five subcells in a string are illuminated, they induce around  $-4.63$  V (Figure S6, Supporting Information) voltage bias on the shaded subcell. As shown earlier (Figure 1b), this reverse-bias is already beyond the breakdown voltage, which explains the observed reverse current in the string, which is not close to zero anymore. Remarkably, none of the subcells displayed any signs of degradation after this experiment (Figure S7, Supporting Information).

Partial shading of a subcell in a string (as opposed to complete shading shown in Figure 3a) is even more critical for device degradation (due to amount of dissipated heat) as it shifts the operating point closer to the maximum power point of the unshaded subcells. Figure 3b shows how much heat would be dissipated in a shaded subcell, with various shaded portions of the subcell. In our C-PSCs, the FF is significantly limited by the long transport distance for holes through the carbon-based electrode, which would not be the case in the complete perovskite modules with carbon-based back-contacts (C-PSMs) due to optimized cell geometry. The simulated heatmap in Figure 3c (based on the simulated module with six cells in Figure S8, Supporting Information) gives an example of the power dissipated as heat as a function of the FF of the nonshaded areas of a module (consisting of only one string with six subcells) and the shading area of the subcell. Both parameters play a significant role in the creation of the so-called “hotspots”—locations with high energy dissipation (as shown in Figure 3c, the power density value varies even over an order of magnitude). In case of C-PSMs with high FFs ( $>70\%$ ), the power dissipated as heat in a 5% shaded subcell can reach values above  $1 \text{ W cm}^{-2}$  of the shaded area, meaning that if a subcell, for example, has a size of  $100 \text{ cm}^2$  there will

be 5 W of power dissipated as heat in the shaded  $5 \text{ cm}^2$  area, i.e.,  $1 \text{ W cm}^{-2}$ , which is the power equivalent to 10 suns (referring to the standard AM1.5G spectrum).

### 2.3. Identifying the Critical Reverse-Bias Voltage in C-PSCs

Up to now, despite the applied high reverse-bias voltages, we do not observe any signs of degradation in C-PSCs. However, as it is reasonable to assume that strings in large-scale PSMs would have more than ten subcells, the reverse-bias voltage can easily go beyond 10 V (assuming the  $V_{OC}$  of each subcell is at least 1 V). Even in silicon-based PV modules, where the breakdown voltage is typically at around  $-13 \text{ V}$ ,<sup>[45–47]</sup> bypass diodes are included for every series-interconnected string of 20–24 cells, to prevent the reverse-bias voltages during shading of reaching values close to junction breakdown value.

We expect that reverse-bias-induced device failure is a function of both applied bias and dwell time at this bias point. Therefore, we measured the current of single cells at fixed negative voltage values for different dwell times (Figure 4a). Instantly after applying the reverse-bias, the current sharply increases, followed by the slower decrease and stabilization, which will be discussed in the following section.

Figure 4b shows the PCE change in the C-PSCs depending on the value and duration of the applied reverse-bias. Surprisingly, the cells exhibit outstanding resilience to reverse-bias degradation, showing no significant losses even after biasing with  $-9 \text{ V}$  for as long as 30 min. When a voltage of  $-10 \text{ V}$  is applied, PCE starts to rapidly decrease and after a bias of  $-11 \text{ V}$  (Figure S9, Supporting Information, for  $-11 \text{ V}$ ), the cells show drastic degradation. As can be seen from the photographs in Figure S10, Supporting Information, higher applied negative bias leads to a decrease in absorption in the visible light spectrum and the emergence of yellow regions which, as confirmed by the X-ray diffraction (XRD) measurement (Figure S11, Supporting Information), can be attributed to the (partial) decomposition from perovskite to  $\text{PbI}_2$ . This, in turn, reduces the device active



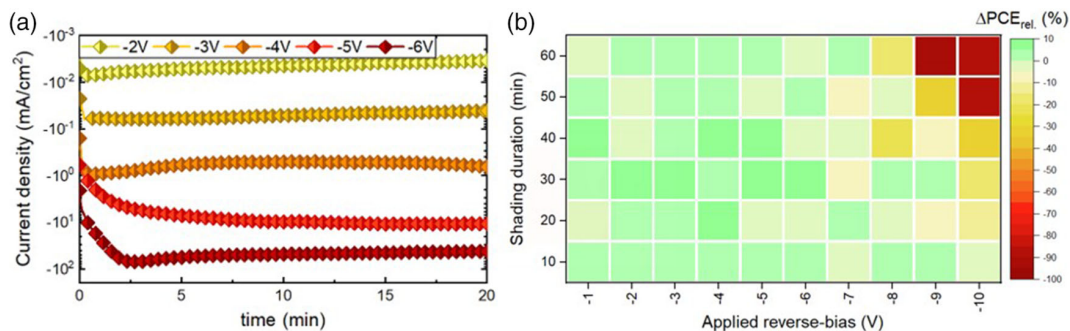


**Figure 4.** a) Current of the cell in the dark as a function of time under reverse-bias (–1 to –6 V), thus mimicking the shading of subcell in a module. Note that the scale is logarithmic because the current increases exponentially under reverse-bias. b) The change in PCE of C-PSCs before and after applying reverse-bias (–1 to –10 V) for a specific time duration (10–60 min) in the dark.

area, which leads to a decrease in the  $I_{SC}$  and therefore overall device PCE.

#### 2.4. Reverse-Bias Behavior of Perovskite Solar Cells and Origins of Degradation

In semiconductor devices, the junction breakdown typically occurs via one of the following three mechanisms: 1) thermal runaway (also known as thermal instability); 2) tunneling; or 3) avalanche multiplication. Normally, for junctions with breakdown voltages  $V_{br} > 6 E_g/q$ , the breakdown can be attributed to impact ionization leading to avalanche multiplication, whereas for  $4 E_g/q < V_{br}$  the breakdown happens due to tunneling effect. For  $4 E_g/q < V_{br} < 6 E_g/q$  the breakdown is assumed to happen by the interplay of both mechanisms.<sup>[37]</sup>

As the bandgap of the  $\text{CH}_3\text{NH}_3\text{PbI}_3$ -based perovskite utilized in this study is approximately 1.6 eV<sup>[48]</sup> and  $V_{br} < 4$  V, the junction breakdown probably occurs first via tunneling, followed by the thermal runaway. It was previously observed that in PSCs thermal runaway causes localized heating of the metal back-contact, causing electrode melting (e.g., silver).<sup>[33]</sup> In addition, Razera et al. also mentioned that the localized shunting induced by reverse-bias may originate from the metal ion migration toward the perovskite layer.<sup>[34]</sup> Moreover, phase segregation in the mixed perovskite compositions (multication and multihalide) was suggested to play a role in the reverse-bias degradation.<sup>[34]</sup> It is clear that the metallic contact-induced degradation (electrode melting and metal ion migration) does not happen in C-PSCs and as the perovskite composition utilized in this work consists of only one A-site cation and one type of halide, phase segregation can also be excluded. We also note that larger thickness of intrinsic i) region of the C-PSCs, where perovskite is embedded in  $\text{ZrO}_2$ , is likely to reduce the electric field and electric potential gradients in comparison with the standard PSCs thinner perovskite films. This, in turn, could result in lower local charge densities, decrease tunneling probability, and increase breakdown voltage (more details can be found in the Supplementary Note 1). However, we note that a more detailed investigation is needed to accurately determine whether the main improvements against reverse-bias-induced degradation come from the presence of carbon electrode or the mesoscopic structure.

##### 2.4.1. Degradation Due to Iodine Loss

An increase in the applied negative voltage results in stronger band bending and thus electric field, which leads to redistribution of mobile ions from perovskite bulk toward its interfaces to charge-extracting layers.<sup>[36]</sup> Bowring et al. have earlier suggested that the initial sharp current increase under fixed reverse-bias, similar to what we demonstrated in Figure 4a, is due to rapid cation (most likely iodine vacancies in  $\text{CH}_3\text{NH}_3\text{PbI}_3$ -based perovskites<sup>[49–53]</sup>) movement toward the interface between the HSL and perovskite.<sup>[33]</sup> In the case of our HSL-free C-PSCs, these iodine vacancies will accumulate at the perovskite/carbon contact, which, in turn, produces a region with an excess of anions close to the ESL/perovskite interface.<sup>[36]</sup> Increase in the band bending at this interface reduces potential barrier width between the conduction band of ESL and valence band of perovskite, allowing holes to tunnel to perovskite.<sup>[33]</sup> Higher hole densities, in relation to electron densities, could result in oxidation of iodide and creation of iodine vacancies and interstitials.<sup>[49,54,55]</sup> Furthermore, created iodine interstitials will undergo structural relaxations toward more thermodynamically favorable iodine compounds such as  $\text{I}_2$  and  $\text{I}_3^{2-}$ .<sup>[49]</sup> Their formation in perovskites under illumination was already demonstrated experimentally<sup>[49,56]</sup> and was found to negatively affect the device performance.<sup>[57]</sup>

To probe whether molecular iodine is created in our C-PSCs under reverse-bias, we submerge a solar cell in toluene (2 mL) while applying –3 V bias to it (Figure S12, Supporting Information) in the dark. After 24 h, the toluene was extracted to measure its UV–vis absorption spectrum. As shown in Figure S13a, Supporting Information, in comparison with a cell which underwent the same treatment but without an applied bias, the absorption is strongly increased in 300–400 nm wavelength region and a characteristic peak of  $\text{I}_2$  at  $\approx 500$  nm appeared. Similar behavior was observed for iodine dissolved in toluene<sup>[58]</sup> and iodine compounds formed in perovskites under illumination.<sup>[49,56]</sup> The absorption of iodine dissolved in toluene (Figure S13b, Supporting Information) shows strong absorption in those wavelength regions, confirming our hypothesis. Moreover, the photograph in Figure S12, Supporting Information, shows strong change in light-absorbing properties inside the perovskite active area of cells which were under

reverse-bias in toluene. For comparison, a cell also kept in toluene for 24 h but under open-circuit condition did not show any visible changes in the active area. Furthermore, the cell subjected to reverse-bias does not show visible degradation in the “dead area” between the laser lines, confirming further that the degradation is bias-induced. Thus, we can clearly see that even though C-PSCs can withstand low reverse-bias for a short time (<1 h) without a drop in performance, prolonged applied negative voltages cause significant iodine loss from perovskite crystal structure, which will be detrimental for the device lifetime.

#### 2.4.2. Degradation Due to Excessive Heating

To elucidate the causes of degradation mechanisms in C-PSCs happening at large negative voltages, we perform real-time infrared imaging. Thermal radiation is detected with an infrared camera, while a bias voltage is applied to the device in the dark.

At low reverse-bias (for the shown device  $> -7$  V) we do not observe a significant inhomogeneity in cell temperature except for a local shunt (**Figure 5a**). Here, we define shunts as regions with reduced shunt resistance due to printing defects/pinholes or artifacts, causing excessive localized heating of the device under reverse-bias. However, once a high reverse-bias is applied (e.g.,  $\leq -7$  V) the temperature at the shunt and neighboring region increases dramatically, which leads to perovskite degradation. This strong increase in temperature is caused by a strong increase in reverse current. Notably, we note a peculiar feature, where after the local degradation at the shunt location, the “hotspot” moves toward the region close to the P1 laser line (located at the upper part of the cell), followed by moving further along the laser line and regions close to it. After about 19 s, the hotspot vanishes and the power is again dissipated almost evenly throughout the area of the cell (although some spots still appear hotter than others). The vanishing of the hotspot is accompanied

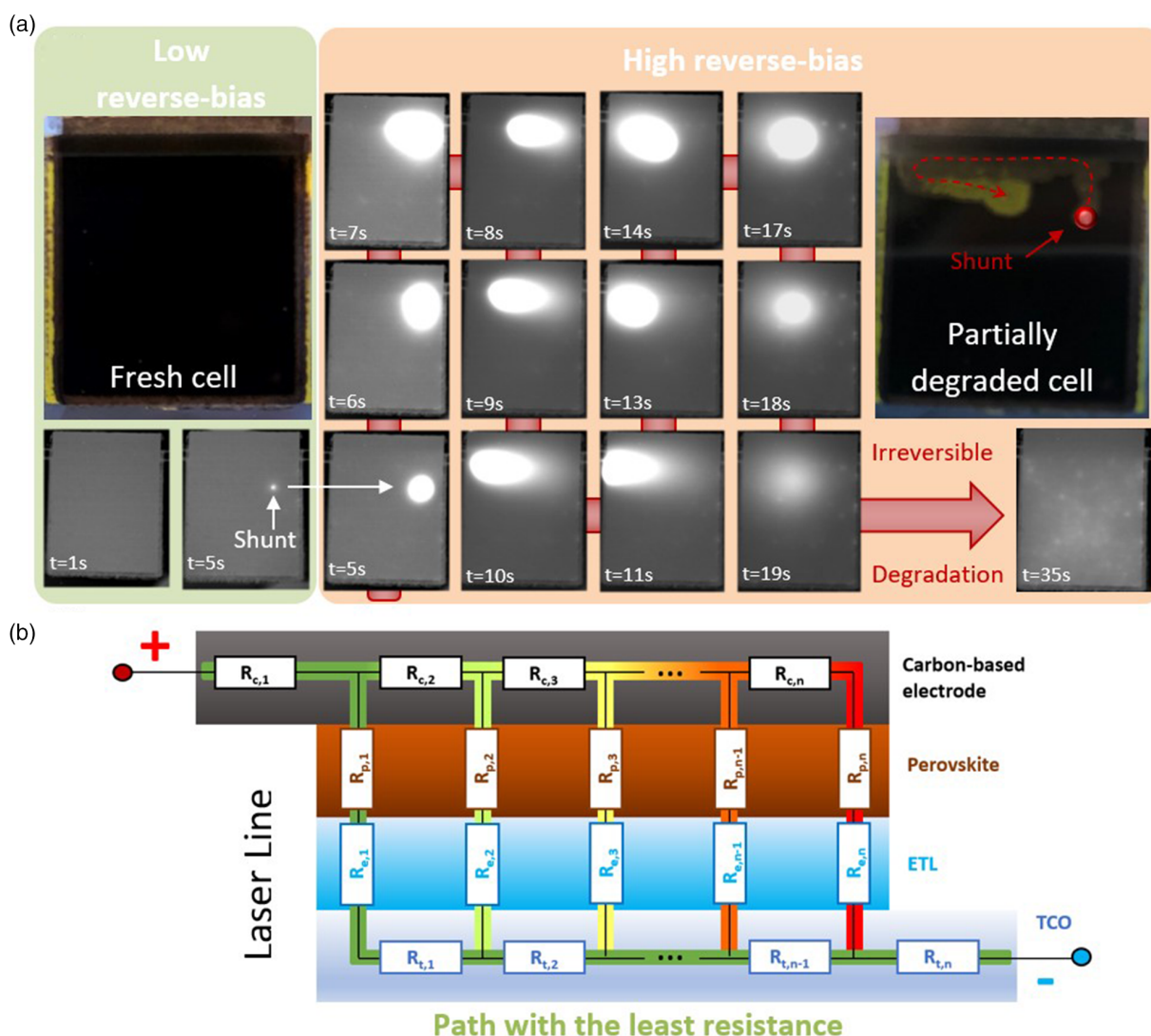


**Figure 5.** a) Infrared thermography measurements at low and high applied negative biases, showing that in shunted cells, the degradation starts at the location of a shunt, leading to overheating and decomposition of perovskite. b) Proposed electrical circuit model to explain the hotspot movement resulting in partial degradation of C-PSCs.

by a decrease in reverse current. The entire real-time infrared measurement showing the degradation process can also be found in Video S1, Supporting Information. Looking at the active area we can see a strong correlation between the hotspot “path” and the degraded regions of the cell, from which we could also reconstruct the degradation path. Here, the degradation might have been caused by two mechanisms: 1) the rate of iodide oxidation is increased leading to higher iodine loss; and/or 2) heat up of perovskite beyond its decomposition temperature.<sup>[59]</sup> Further investigation is needed to specifically resolve this ambiguity and pinpoint the main origin of the degradation under reverse-bias in such solar cells. We note, however, that under a bias of  $-9\text{ V}$  overall cell temperature (not localized) can reach temperatures close to  $100\text{ }^{\circ}\text{C}$  (Figure S14, Supporting Information), suggesting that degradation of the  $\text{CH}_3\text{NH}_3\text{PbI}_3$ -based perovskite is likely to occur at such voltage levels. For the local hotspots as shown in Figure 5a, the dark lock-in thermography (DLIT) signal exceeded the detector range and it is reasonable that the power dissipated at the small spots induces a much higher local heating. Nevertheless, as shown in Figure S15, Supporting Information, after the reverse-bias is applied to the shunted cell, the degradation does not progress unless the applied bias is above  $-9\text{ V}$ . Once, it happens, most of the active area rapidly heats up (Figure S15 and Video S2, Supporting Information), turning yellow, suggesting the formation of  $\text{PbI}_2$  across most of the active area. We note, however, that some XRD peaks corresponding to perovskite reflection planes (e.g., (220), (211)) can still be observed in the degraded samples.

To explain why the hotspots occur primarily close to the laser line, we propose the electrical circuit model shown in Figure 5b. Assuming that the resistance of the perovskite and  $\text{m-TiO}_2$  layer is nearly constant across the active area, the path of the least resistance for current is dictated by the resistance of the front- and back-electrodes. According to our 4-point probe measurements, the sheet resistance of the carbon-based electrode and FTO is around  $18 \pm 2$  and  $8.5 \pm 1.5\ \Omega\ \text{sq}^{-1}$ , respectively, demonstrating that there are more resistive losses in the back-contact rather than in the front-electrode.<sup>[48]</sup> This suggests that the current path with the least resistance (marked with green color in Figure 5b) contains minimal distance through the back-electrode (carbon) and

maximal distance through the front-electrode (FTO). Clearly, such path goes through regions close to the laser line, which is why the DLIT signal increases at this location first (as seen from Video S1, Supporting Information). The high current at these spots leads to local heating, causing thermal decomposition of the perovskite into  $\text{PbI}_2$ , most likely due to evaporation of the more volatile methylammonium iodide.<sup>[59]</sup> As the residual  $\text{PbI}_2$  is less conductive than the pristine perovskite at the surrounding areas, another location becomes the path of least resistance. The local heating makes it likely that this location is neighboring the “just-degraded” spot. However, we highlight that if shunts are present, degradation will first happen at the shunt because it is the path of least resistance. After the perovskite near the shunt degrades, the hotspot will appear close to the laser line. However, these regions will not degrade because they are shunted, but because these locations represent the path of least resistance for the current.

As we pointed out, the location of the initial degradation (in the absence of shunts) depends on the electrode sheet resistivities and their relation to each other. That means if the electrode sheet resistances were equal, the degradation would occur more homogeneously across the active area because the current flow would be distributed more homogeneously across the cell area, and so would the heat.

#### 2.4.3. Hotspot Test of Perovskite Solar Modules with Carbon-Based Electrodes

Inspired by the outstanding stability of the individual cells to negative voltage bias, we manufactured perovskite minimodules with carbon-based back-contacts on a  $10 \times 10\ \text{cm}^2$  FTO substrate. Figure 6a shows a photograph of the encapsulated C-PSM with a  $56.8\ \text{cm}^2$  aperture area and a geometrical FF of 93.4%. From the  $I$ - $V$  measurement the power conversion efficiency of the module was determined to be 11.1% (reverse sweep).

To pass the “hotspot test” described in the IEC 61215-2:2016 standard, a PV module needs to be subjected to a partial shading representing the “worst case” shading and operation conditions.<sup>[19]</sup> In general, there are two different types of hotspot tests that are applied to PV modules: 1) test for silicon wafer-based

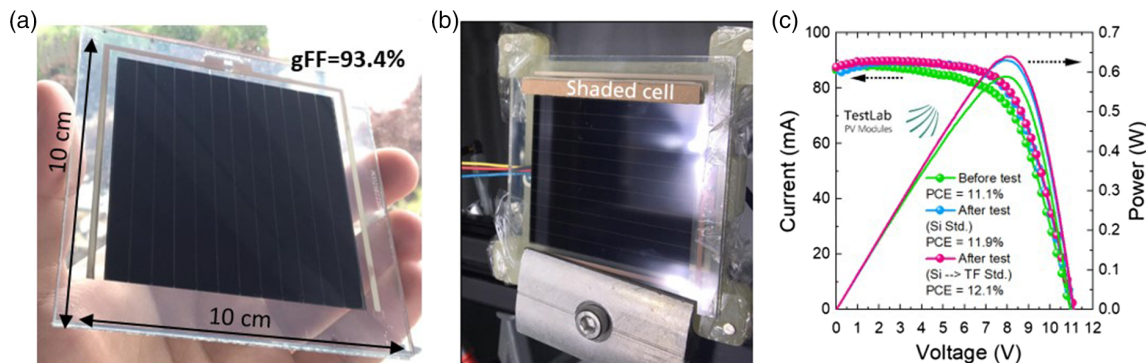


**Figure 6.** a) Photograph of an encapsulated perovskite solar module with carbon-based contact (C-PSM). b) Photograph of the module with one fully shaded cell during the hotspot test. Shading conditions c)  $I$ - $V$  and  $P$ - $V$  curves of the module before (green) and after conducting test according to silicon ageing test (blue), followed by conducting an additional thin-film ageing test (cerise) on the same module, showing no loss of performance after both IEC-compliant tests.



(IEC 61 215-2, MQT 09.1) modules; and 2) test for thin-film technologies (IEC 61215-2, MQT 09.2). The key difference between both tests is the presence of the partial shading condition: MQT 09.2 test only requires full shading of one or more subcells, whereas for MQT 09.1 the full subcell area shading is followed by an additional partial shading of a subcell (as will be shown later). As discussed earlier (and shown in Figures 3b,c), partial shading of a subcell can be more detrimental, and the closer the operating point of the module to the maximum power point (MPP), the more power will be dissipated as heat. As for the tested module, the partial shading conditions lead to operation close to the MPP, highlighting that the MQT 09.1 is a harsher test and is more likely to result in module deterioration. Nevertheless, due to the lack of a standard specifically for the perovskite PV modules, both tests (MQT 09.1 and MQT 09.2) were applied sequentially on the same module at an accredited laboratory “TestLab PV Modules” at Fraunhofer ISE.<sup>[19]</sup>

According to the standardized procedure MQT 09.1, after measuring the  $I$ - $V$  curve of our C-PSM (without shading) we fully shade each individual subcell (Figure 6b) and obtain the module  $I$ - $V$  curve when each cell is fully shaded (Figure S16, Supporting Information). From these curves, a cell with the lowest shunt resistance is identified, suggesting that this cell might have the highest chance to rapidly heat up at the shunt location under shading conditions. The shaded area of the cell with the least shunt resistance was reduced from 100% to 25%, and the condition resulting in the highest temperature was held for 1 h. Subsequently, the procedure for thin-film modules (MQT 09.2) was conducted in which the shading of one or more cells was adjusted so that the  $I_{SC}$  of the shaded module is equal to the  $I_{MPP}$  of the nonshaded module. This condition was again sustained for 1 h. More details on the testing procedures,  $J$ - $V$  curves of C-PSM under different shading conditions, and infrared temperature measurements can be found in the hotspot test report in the Supporting Information.

The maximum temperature observed was below 50 °C in both tests. The module passed the criteria of visual inspection and  $I$ - $V$  curve characteristics after both shading conditions. As can be clearly seen from Figure 6c, the module does not exhibit significant signs of degradation after the test, and the PCE has, in fact, slightly enhanced. To confirm this performance improvement, we track the PCE of the module for 1 h under full sun illumination (Figure S17, Supporting Information), which also shows that the aged device has a higher stabilized PCE. This agrees with our previously shown results of individual C-PSCs subjected to constant negative voltages in Figure 4b, where the cell PCE often slightly increases if the reverse-bias is below -8 V. Although the results suggest that these C-PSMs have a sufficient stability to withstand the reverse operating conditions during the hotspot test, e.g., in the context of module certification, the module size and encapsulation could change during the still ongoing module development, which is why the insulation criteria, specified in the IEC 61215-2, were not applied during the test. The relatively low temperatures measured (<50 °C) can be attributed, in part, to the small cell sizes and the resulting low power that is dissipated under shading conditions. Therefore, the test could yield different results for modules with larger cells or longer cell strings and should be reassessed in these cases.

### 3. Conclusion

Although preventing degradation of perovskite photovoltaic devices is commonly considered a cornerstone of commercialization of PV modules of this technology, there are only few studies on the degradation under reverse-bias conditions, indicating that this could be an Achilles heel for PSCs. In this work, we address this fundamental problem and demonstrate that perovskite solar cells with carbon-based electrodes are remarkably resilient against reverse-bias stress. These cells have a breakdown voltage at approximately -3.6 V, suggesting that the junction breakdown occurs via tunneling. As carbon-based electrodes are not prone to melting at high temperature, neither to migration of (metal) ions from the electrode into perovskite absorber, nor to electrode oxidation, they represent an ideal candidate for improving the stability of PSCs under reverse-bias conditions. Moreover, the stability of cells demonstrated here is further improved by the utilization of single-cation and single-halide perovskite, avoiding phase segregation. These advantages allow PSCs with carbon-based electrodes to withstand at least 60 min under -8 V and 30 min at -9 V. We demonstrate, however, that the C-PSCs undergo iodine loss under even mild negative voltages, due to tunneling of holes, which oxidize iodide incorporated into perovskite lattice and form iodine compounds. However we note that this reaction might be reversible, unlike degradation which happens under high reverse-bias. By real-time infrared thermography measurement, we show that the degradation at high negative voltages starts in shunts, where heat is dissipated. After that (or in the absence of shunts), the degradation follows the current path of least resistance, which depends on the sheet resistances of front- and back-electrodes. Combining these findings with the XRD measurements we demonstrate that the main mechanism leading to the degradation of C-PSCs under high reverse-bias is conversion of perovskite to  $PbI_2$  at high temperatures. Finally, we manufactured perovskite modules with 56.8 cm<sup>2</sup> aperture area and subjected them to the “hotspot” stability test at an accredited laboratory, “TestLab PV Modules” at Fraunhofer ISE. For the first time, we show perovskite modules which endure the IEC 61215-2:2016 standard test procedures, underlining excellent potential of such modules for commercialization. Finally, we highlight that further improvement of the standardization of the hotspot tests for perovskite (single- and multijunction) modules is needed to accurately assess the long-term stability of such PV devices.

### 4. Experimental Section

**Materials:** Fluorine-doped tin oxide glass substrates TCO22-7/LI (sheet resistance 7  $\Omega$  sq<sup>-1</sup>), silver paste Elcosil SG/SP, titania paste Titanoxide T165/SP, zirconia paste Zr-nanoxide ZT/SP, carbon-graphite paste Elocarb B/SP and methylammonium lead iodide perovskite solution with 5-ammonium valeric acid additive (5-AVAI) were provided by Solaronix SA. Acetone was purchased from Carl-Roth, and ethanol was purchased from Alcosuisse. Titanium diisopropoxide bis(acetylacetonate) (75% in isopropanol), and Hellmanex and isopropanol were purchased from Sigma-Aldrich.

**Fabrication of Perovskite Solar Cells with Carbon-Based Electrodes:** Devices were fabricated on 10 × 10 cm<sup>2</sup> plates of FTO-coated glass. First, a laser pattern defined cathode and anode areas with an automated



fiber laser. After that, the substrate was subjected to sequential cleaning steps in 1% aqueous solution of Hellmanex, acetone, and isopropanol respectively (15 min each) in an ultrasonic bath and subsequently dried in air. The thin compact titania layer (c-TiO<sub>2</sub>) was grown by spray-pyrolysis on a hot-plate set to 450 °C, using a glass mask to protect the contact areas. A volume of 20 mL of titanium diisopropoxide bis(acetylacetonate) diluted in absolute ethanol (1:160) was sprayed with oxygen as a carrier gas, and warming was prolonged for 30 min before allowing the sample to cool down. For the manufacturing of C-PSCs, an array of 18 electrodes was subsequently defined by screen-printing silver contacts, m-TiO<sub>2</sub>, ZrO<sub>2</sub>, and carbon paste using a 100–40, 165–30, 90–48, and 43–80 mesh stencil, respectively (the number of strands is per cm). After printing the wet film, each screen-printed layer was allowed to dwell for 10 min before drying at 120 °C for 10 min, followed by a firing step at 500 °C (or 400 °C for carbon) for 30 min, after a 30 min ramp.

The freshly fired electrodes were masked with an adhesive polyimide gasket (provided by Solaronix) to delimit the wet area. The perovskite precursor was redissolved at 70 °C right prior to use. An empirically determined volume of 5.76 µL of the perovskite precursor solution was dropped in the center of each electrode using a micropipette. The infiltration of the perovskite ink was done using a home-made semiautomated dispensing system.

Same processes were used to manufacture C-PSMs with 12 series-interconnected cells except for the aperture area of the screen-printing mesh and perovskite filling procedure. The infiltration of the modules with perovskite solution was conducted via inkjet-filling process with a 10 pL droplet volume and 1200 × 1200 dpi resolution.

The wet samples (cells and modules) were then moved to an oven set to 50 °C where they were dried for 60 min, thus forming the perovskite crystals in the porous electrode structure. The polyimide adhesive gasket was carefully peeled off, and the solar cells were individualized by cutting the glass substrate into the corresponding solar cells. The resulting devices were submitted to heat and damp treatment at 40 °C and 75% RH for 150 h, according to the previously reported method by Hashmi et al.<sup>[60]</sup>

**Characterization:** The current density and voltage curves of solar cells were measured with a source meter (Keithley 2400) at a scan rate of 20 mV s<sup>-1</sup> using a class A solar simulator providing 100 mW cm<sup>-2</sup>, AM1.5G illumination. Same equipment was used for obtaining *I*-*V* curves of the modules, but the scan rate was set to 100 mV s<sup>-1</sup> in this case. The current measurement of a cell without illumination at a fixed voltage for specific time durations has been measured with the same source meter. After this measurement, slow *V*<sub>OC</sub> recovery process is observed (as mentioned in the main text), which depends on the magnitude of applied reverse-bias. For the reason of objective comparison, the cells were measured the next day, to determine the performance change after the applied bias for specific time duration. Sheet resistance of front- and back-electrodes was measured in several places with a 4-pin probe sheet resistance meter Guardian Manufacturing SRM-232-100. The light reflection, transmission, and absorption were measured with Perkin Elmer Lambda 950 UV-vis/NIR spectrophotometer with an integrating sphere. XRD diffraction patterns were recorded at room temperature with an XPERT-3 MRD system using a Xe point detector, Bragg-Brentano beam optics, and a Cu K $\alpha$  radiation source. Diffraction spectra were recorded between  $2\theta = 5^\circ$  and  $2\theta = 65^\circ$  at a scan rate of 1.5° min<sup>-1</sup> with a step size of 0.015°. The setup used for DLIT characterization was a custom-made tool by the company IRCAM GmbH. The camera contained an InSb-based midwave infrared focal plane array (MWIR FPA) detector, sensitive to IR radiation in the range of 1.5–5 µm, and was actively cooled. The solar cell was subjected to bias voltage of a Toellner four-quadrant power supply and the IR camera signal was analyzed as a real-time video. For the measurements of cell temperature over the whole active area, a thermometer-set Qtemp 200 (manufactured by VWR International GmbH) was utilized.

Details on the characterization of modules during the IEC IEC61215-2 MQT 09.1 and MQT 09.2 can be found in the hotspot test report in the Supporting Information.

## Supporting Information

Supporting Information is available from the Wiley Online Library or from the author.

## Acknowledgements

This work has been partially funded within the projects PROPER financed from the German Ministry of Education and Research under funding number 01DR19007 and UNIQUE supported under umbrella of SOLAR-ERA.NET\_cofund by ANR, PtJ, MIUR, MINECO-AEI, and SWEA, within the EU's HORIZON 2020 Research and Innovation Program (cofund ERA-NET Action No. 691664). D.B. acknowledges the scholarship support of the German Federal Environmental Foundation (DBU) and S.Z. acknowledges the scholarship support of the German Academic Exchange Service (DAAD). This material is based upon work supported by the U.S. Department of Energy's Office of Energy Efficiency and Renewable Energy (EERE) under Solar Energy Technologies Office (SETO) Agreement Number DE-EE0008551.

Open access funding enabled and organized by Projekt DEAL.

## Conflict of Interest

M.M. is an advisor to Swift Solar. D.M., S.N., and A.V. are employees of Solaronix SA.

## Author Contributions

D.B., D.M., and L.W. have conceived the idea of this publication. D.B. coordinated the work, analyzed all the measurements, and prepared the manuscript, as well as Figures D.M., S.N., and A.V. manufactured perovskite solar cells and modules with carbon-based contacts (C-PSCs and C-PSMs). D.B., L.W., and S.Z. created a numerical simulation of series-interconnected subcells of C-PSCs. J.H. performed IR thermographic measurement. L.W. and D.B. developed an electrical circuit model to explain the device behavior observed from thermographic measurements. K.S. and D.B. measured the *J*-*V* characteristics of all the manufactured solar cells. N.G. performed XRD measurements and D.B. conducted UV-vis measurements. J.M. performed the official "hotspot" test at the accredited laboratory "TestLab PV Modules" at Fraunhofer ISE and P.G. analyzed the results and prepared the hotspot test report, as well as part of the manuscript corresponding to the IEC 61215-2:2016 test description. L.W., S.Z., U.W., A.H. I.G., and M.M. provided important conceptual ideas, and contributed to the manuscript preparation and results interpretation. All authors have made valuable comments to the manuscript.

## Data Availability Statement

Research data are not shared.

## Keywords

degradation, IEC 61215:2016, perovskites, reverse-bias, shading, solar cells, solar modules

Received: July 12, 2021

Revised: September 14, 2021

Published online: October 13, 2021

- [1] Y.-H. Kim, J. S. Kim, T.-W. Lee, *Adv. Mater.* **2019**, *31*, e1804595.
- [2] S. P. Senanayak, M. Abdi-Jalebi, V. S. Kamboj, R. Carey, R. Shivanna, T. Tian, G. Schweicher, J. Wang, N. Giesbrecht, D. Di Nuzzo, H. E. Beere, P. Docampo, D. A. Ritchie, D. Fairen-Jimenez, R. H. Friend, H. Sirringhaus, *Sci. Adv.* **2020**, *6*, eaaz4948.
- [3] K. Liao, X. Hu, Y. Cheng, Z. Yu, Y. Xue, Y. Chen, Q. Gong, *Adv. Opt. Mater.* **2019**, *7*, 1900350.
- [4] J.-P. Correa-Baena, M. Saliba, T. Buonassisi, M. Grätzel, A. Abate, W. Tress, A. Hagfeldt, *Science* **2017**, *358*, 739.
- [5] Y. Rong, Y. Hu, A. Mei, H. Tan, M. I. Saidaminov, S. I. Seok, M. D. McGehee, E. H. Sargent, H. Han, *Science* **2018**, *361*, eaat8235, <https://doi.org/10.1126/science.aat8235>.
- [6] M. Saliba, J.-P. Correa-Baena, M. Grätzel, A. Hagfeldt, A. Abate, *Angew. Chem.* **2018**, *57*, 2554.
- [7] J. Y. Kim, J.-W. Lee, H. S. Jung, H. Shin, N.-G. Park, *Chem. Rev.* **2020**, *120*, 7867.
- [8] C. M. Wolff, P. Caprioglio, M. Stolterfoht, D. Neher, *Adv. Mater.* **2019**, *31*, e1902762.
- [9] J. Jeong, M. Kim, J. Seo, H. Lu, P. Ahlawat, A. Mishra, Y. Yang, M. A. Hope, F. T. Eickemeyer, M. Kim, Y. J. Yoon, I. W. Choi, B. P. Darwich, S. J. Choi, Y. Jo, J. H. Lee, B. Walker, S. M. Zakeeruddin, L. Emsley, U. Rothlisberger, A. Hagfeldt, D. S. Kim, M. Grätzel, J. Y. Kim, *Nature* **2021**, *592*, 381.
- [10] N.-G. Park, K. Zhu, *Nat. Rev. Mater.* **2020**, *5*, 333.
- [11] NREL National Renewable Energy Laboratory, Efficiency Chart, **2021**, <https://www.nrel.gov/pv/cell-efficiency.html>.
- [12] M. Green, E. Dunlop, J. Hohl-Ebinger, M. Yoshita, N. Kopidakis, X. Hao, *Prog. Photovoltaics Res. Appl.* **2021**, *29*, 3.
- [13] Q. Wang, N. Phung, D. Di Girolamo, P. Vivo, A. Abate, *Energy Environ. Sci.* **2019**, *12*, 865.
- [14] K. Domanski, J.-P. Correa-Baena, N. Mine, M. K. Nazeeruddin, A. Abate, M. Saliba, W. Tress, A. Hagfeldt, M. Grätzel, *ACS Nano* **2016**, *10*, 6306.
- [15] J. M. Frost, K. T. Butler, F. Brivio, C. H. Hendon, M. van Schilfgaarde, A. Walsh, *Nano Lett.* **2014**, *14*, 2584.
- [16] J. Huang, S. Tan, P. D. Lund, H. Zhou, *Energy Environ. Sci.* **2017**, *10*, 2284.
- [17] F. Li, M. Liu, *J. Mater. Chem. A* **2017**, *5*, 15447.
- [18] D. Bogachuk, S. Zouhair, K. Wojciechowski, B. Yang, V. Babu, L. Wagner, B. Xu, J. Lim, S. Mastroianni, H. Pettersson, A. Hagfeldt, A. Hinsch, *Energy Environ. Sci.* **2020**, *13*, 3880.
- [19] International Electrotechnical Commission (IEC), *IEC 61215-2:2016: Terrestrial Photovoltaic (PV) Modules - Design Qualification and Type Approval - Part 2: Test Procedures*, <https://webstore.iec.ch/publication/24311> (accessed: May 2021).
- [20] P. Holzhey, M. Saliba, *J. Mater. Chem. A* **2018**, *6*, 21794.
- [21] A. Mei, Y. Sheng, Y. Ming, Y. Hu, Y. Rong, W. Zhang, S. Luo, G. Na, C. Tian, X. Hou, Y. Xiong, Z. Zhang, S. Liu, S. Uchida, T.-W. Kim, Y. Yuan, L. Zhang, Y. Zhou, H. Han, *Joule* **2020**, *4*, 2646.
- [22] R. Cheacharoen, K. A. Bush, N. Rolston, D. Harwood, R. H. Dauskardt, M. D. McGehee, in *2018 IEEE 7th World Conf. on Photovoltaic Energy Conversion (WCPEC): (A Joint Conf. of 45th IEEE PVSC, 28th PVSEC & 34th EU PVSEC)*, IEEE, Piscataway, NJ June 2018, p. 3498.
- [23] R. Cheacharoen, C. C. Boyd, G. F. Burkhard, T. Leijtens, J. A. Raiford, K. A. Bush, S. F. Bent, M. D. McGehee, *Sustainable Energy Fuels* **2018**, *2*, 2398.
- [24] L. Shi, M. P. Bucknall, T. L. Young, M. Zhang, L. Hu, J. Bing, S. Da Lee, J. Kim, T. Wu, N. Takamura, D. R. McKenzie, S. Huang, M. A. Green, A. W. Y. Ho-Baillie, *Science* **2020**, *368*, eaba2412, <https://doi.org/10.1126/science.aba2412>.
- [25] S. Bai, P. Da, C. Li, Z. Wang, Z. Yuan, F. Fu, M. Kawecki, X. Liu, N. Sakai, J. T.-W. Wang, S. Huettnner, S. Buecheler, M. Fahlman, F. Gao, H. J. Snaith, *Nature* **2019**, *571*, 245.
- [26] N. Arora, M. I. Dar, A. Hinderhofer, N. Pellet, F. Schreiber, S. M. Zakeeruddin, M. Grätzel, *Science* **2017**, *358*, 768.
- [27] A. Mei, X. Li, L. Liu, Z. Ku, T. Liu, Y. Rong, M. Xu, M. Hu, J. Chen, Y. Yang, M. Grätzel, H. Han, *Science* **2014**, *345*, 295.
- [28] Y. Hu, S. Si, A. Mei, Y. Rong, H. Liu, X. Li, H. Han, *Sol. RRL* **2017**, *1*, 1600019.
- [29] W. Chen, Y. Wu, Y. Yue, J. Liu, W. Zhang, X. Yang, H. Chen, E. Bi, I. Ashraf, M. Grätzel, L. Han, *Science* **2015**, *350*, 944.
- [30] R. Shang, Z. Zhou, H. Nishioka, H. Halim, S. Furukawa, I. Takei, N. Ninomiya, E. Nakamura, *J. Am. Chem. Soc.* **2018**, *140*, 5018.
- [31] R. Cheacharoen, N. Rolston, D. Harwood, K. A. Bush, R. H. Dauskardt, M. D. McGehee, *Energy Environ. Sci.* **2018**, *11*, 144.
- [32] F. Bella, G. Griffini, J.-P. Correa-Baena, G. Saracco, M. Grätzel, A. Hagfeldt, S. Turri, C. Gerbaldi, *Science* **2016**, *354*, 203.
- [33] A. R. Bowring, L. Bertoluzzi, B. C. O'Regan, M. D. McGehee, *Adv. Energy Mater.* **2018**, *8*, 1702365.
- [34] R. A. Z. Razera, D. A. Jacobs, F. Fu, P. Fiala, M. Dussouillez, F. Sahli, T. C. J. Yang, L. Ding, A. Walter, A. F. Feil, H. I. Boudinov, S. Nicolay, C. Ballif, Q. Jeangros, *J. Mater. Chem. A* **2020**, *8*, 242.
- [35] J. Qian, M. Ernst, D. Walter, M. A. Mahmud, P. Hacke, K. Weber, M. Al-Jassim, A. Blakers, *Sustainable Energy Fuels* **2020**, *4*, 4067.
- [36] L. Bertoluzzi, C. C. Boyd, N. Rolston, J. Xu, R. Prasanna, B. C. O'Regan, M. D. McGehee, *Joule* **2020**, *4*, 109.
- [37] S. M. Sze, Y. Li, K. K. Ng, *Physics of Semiconductor Devices*, John Wiley & Sons, Hoboken, NJ **2021**.
- [38] A. Smets, K. Jäger, O. Isabella, R. van Swaaij, M. Zeman, *Solar Energy: The Physics and Engineering of Photovoltaic Conversion, Technologies and Systems*, UIT Cambridge, Cambridge **2016**.
- [39] M. Jung, T. J. Shin, J. Seo, G. Kim, S. I. Seok, *Energy Environ. Sci.* **2018**, *11*, 2188.
- [40] B. Conings, J. Drijkoningen, N. Gauquelin, A. Babayigit, J. D'Haen, L. D'Olieslaeger, A. Ethirajan, J. Verbeeck, J. Manca, E. Mosconi, F. de Angelis, H.-G. Boyen, *Adv. Energy Mater.* **2015**, *5*, 1500477.
- [41] G. Grancini, C. Roldán-Carmona, I. Zimmermann, E. Mosconi, X. Lee, D. Martineau, S. Narbey, F. Oswald, F. de Angelis, M. Graetzel, M. K. Nazeeruddin, *Nat. Commun.* **2017**, *8*, 15684.
- [42] D. Kiermasch, L. Gil-Escrig, H. J. Bolink, K. Tvingstedt, *Joule* **2019**, *3*, 16.
- [43] J. W. Bishop, *Solar Cells* **1988**, *25*, 73.
- [44] H. Yang, H. Wang, M. Wang, *Int. J. Photoenergy* **2012**, *2012*, 1.
- [45] O. Breitenstein, J. Bauer, K. Bothe, W. Kwapil, D. Lausch, U. Rau, J. Schmidt, M. Schneemann, M. C. Schubert, J.-M. Wagner, W. Warta, *J. Appl. Phys.* **2011**, *109*, 71101.
- [46] S. Wendlandt, A. Giese, A. Drobisch, D. Tornow, M. Hanusch, J. Berghold, S. Krauter, P. Grunow, in *27th European Photovoltaic Solar Energy Conference*, Frankfurt (Main) **2012**.
- [47] R. G. Vieira, F. M. U. de Araújo, M. Dhimish, M. I. S. Guerra, *Energies* **2020**, *13*, 2472.
- [48] D. Bogachuk, R. Tsuji, D. Martineau, S. Narbey, J. P. Herterich, L. Wagner, K. Suginuma, S. Ito, A. Hinsch, *Carbon* **2021**, *178*, 10.
- [49] G. Y. Kim, A. Senocrate, T.-Y. Yang, G. Gregori, M. Grätzel, J. Maier, *Nat. Mater.* **2018**, *17*, 445.
- [50] A. Senocrate, I. Moudrakovski, G. Y. Kim, T.-Y. Yang, G. Gregori, M. Grätzel, J. Maier, *Angew. Chem.* **2017**, *56*, 7755.
- [51] T.-Y. Yang, G. Gregori, N. Pellet, M. Grätzel, J. Maier, *Angew. Chem.* **2015**, *54*, 7905.
- [52] J. Haruyama, K. Sodeyama, L. Han, Y. Tateyama, *J. Am. Chem. Soc.* **2015**, *137*, 10048.
- [53] E. Mosconi, F. de Angelis, *ACS Energy Lett.* **2016**, *1*, 182.

- [54] G. F. Samu, Á. Balog, F. de Angelis, D. Meggiolaro, P. V. Kamat, C. Janáky, *J. Am. Chem. Soc.* **2019**, *141*, 10812.
- [55] E. J. Wolf, I. E. Gould, L. B. Bliss, J. J. Berry, M. D. McGehee, *Sol. RRL* **2021**, 2100239, 10.1002/solr.202100239.
- [56] S. Chen, X. Xiao, H. Gu, J. Huang, *Sci. Adv.* **2021**, *7*, eabe8130.
- [57] S. Wang, Y. Jiang, E. J. Juarez-Perez, L. K. Ono, Y. Qi, *Nat. Energy* **2016**, *2*, 16195.
- [58] Z.-B. Liu, J.-G. Tian, W.-P. Zang, W.-Y. Zhou, F. Song, C.-P. Zhang, J.-Y. Zheng, H. Xu, *Opt. Lett.* **2004**, *29*, 1099.
- [59] Z. Song, S. C. Watthage, A. B. Phillips, B. L. Tompkins, R. J. Ellingson, M. J. Heben, *Chem. Mater.* **2015**, *27*, 4612.
- [60] S. G. Hashmi, D. Martineau, M. I. Dar, T. T. T. Myllymäki, T. Sarikka, V. Ulla, S. M. Zakeeruddin, M. Grätzel, J. Mater, *Chem. A* **2017**, *5*, 12060.